iScience

CellPress
OPEN ACCESS

Article

Membrane anchoring of the DIRAS3 N-terminal extension permits tumor suppressor function

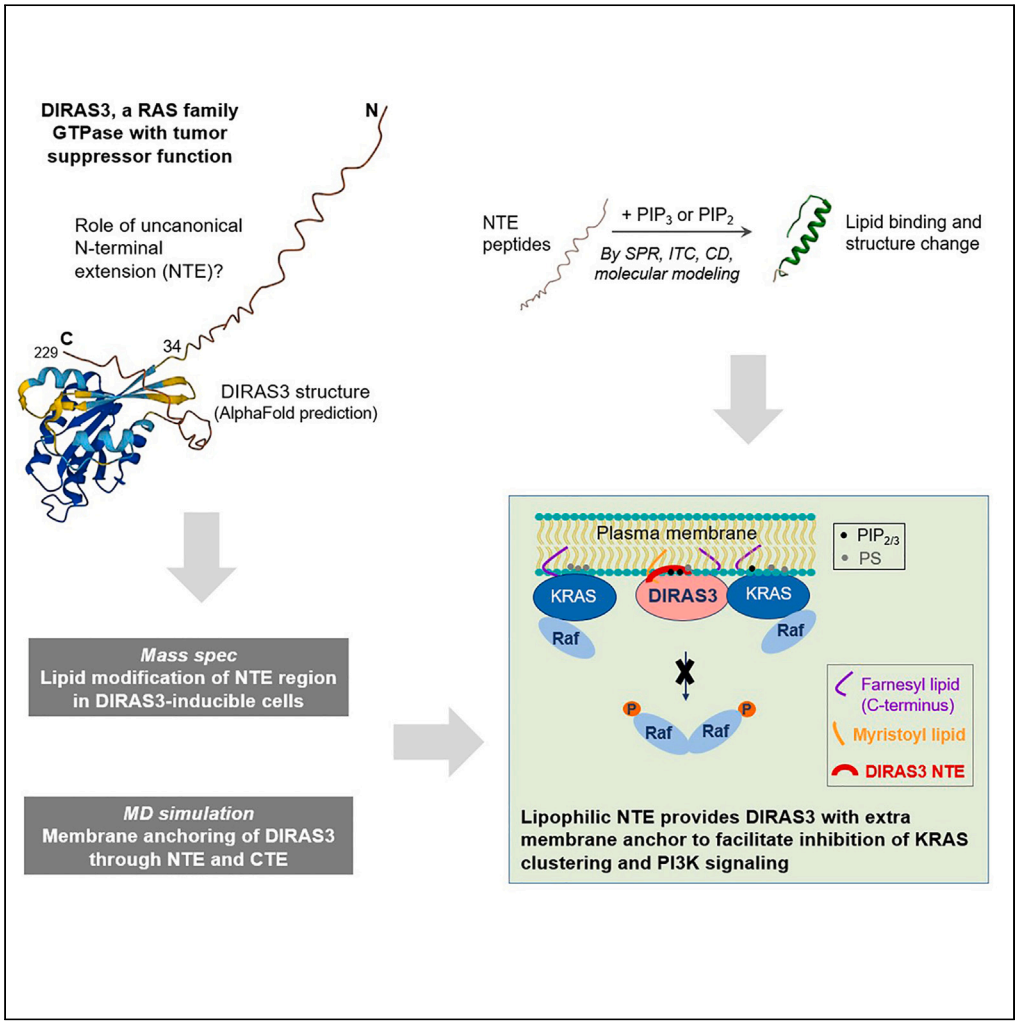

Xiaowen Liang, Sung Yun Jung, Lon Wolf Fong, ..., Yong Zhou, Zhen Lu, Robert C. Bast, Jr.

zlu@mdanderson.org (Z.L.)
rbast@mdanderson.org (R.C.B.)

Highlights

DIRAS3 N-terminal extension (NTE) contains membrane recognition properties

High-affinity NTE-lipid bindings involve disorder to amphipathic helix transition

N-myristoylation of DIRAS3 at NTE is unique among prenylated RAS family GTPase

N- and C-termini double anchors provide stable membrane association to DIRAS3 functions

Liang et al., iScience 26, 108151
November 17, 2023
https://doi.org/10.1016/j.isci.2023.108151

iScience

CellPress
OPEN ACCESS

Article

Membrane anchoring of the DIRAS3 N-terminal extension permits tumor suppressor function

Xiaowen Liang,[1] Sung Yun Jung,[2] Lon Wolf Fong,[1] Gamze Bildik,[1] Joshua P. Gray,[1] Weiqun Mao,[1] Shuxing Zhang,[1] Steven W. Millward,[3] Alemayehu A. Gorfe,[4] Yong Zhou,[4] Zhen Lu,[1,5,*] and Robert C. Bast, Jr.[1,5,6,*]

SUMMARY

***DIRAS3* is an imprinted tumor suppressor gene encoding a GTPase that has a distinctive N-terminal extension (NTE) not found in other RAS proteins. This NTE and the prenylated C-terminus are required for DIRAS3-mediated inhibition of RAS/MAP signaling and PI3K activity at the plasma membrane. In this study, we applied biochemical, biophysical, and computational methods to characterize the structure and function of the NTE. The NTE peptide recognizes phosphoinositides PI(3,4,5)P_3 and PI(4,5)P_2 with rapid kinetics and strong affinity. Lipid binding induces NTE structural change from disorder to amphipathic helix. Mass spectrometry identified N-myristoylation of DIRAS3. All-atom molecular dynamic simulations predict DIRAS3 could adhere to the membrane through both termini, suggesting the NTE is involved in targeting and stabilizing DIRAS3 on the membrane by double anchoring. Overall, our results are consistent with DIRAS3's function as a tumor suppressor, whereby the membrane-bound DIRAS3 can effectively target PI3K and KRAS at the membrane.**

INTRODUCTION

DIRAS3 is an imprinted tumor suppressor gene that encodes a small GTPase with approximately 60% sequence homology to KRAS, differing by the addition of a distinctive N-terminal extension (NTE) that is required for suppressor function.[1,2] Similar to KRAS, DIRAS3 has a conserved catalytic domain responsible for GTP binding and hydrolysis and a C-terminal hypervariable region with a CAAX motif that is prenylated and mediates membrane association of the protein.[2] Downregulation of *DIRAS3* expression was first discovered in ovarian and breast carcinomas by our group[1,3] and later found in other cancer types.[4] Re-expression of DIRAS3 in cancer cells inhibits tumor growth and migration while inducing autophagy and tumor dormancy.[1,2,5,6] Our previous studies demonstrate that DIRAS3 inhibits PI3 kinase activity and membrane localization of phosphorylated AKT.[5] DIRAS3 also inhibits the RAS/MAPK signaling pathway.[2,7,8] Deletion of DIRAS3's unique N-terminal extension (NTE) abolished its inhibitory function, suggesting that the NTE is required for DIRAS3's tumor suppressor functions.

Recently, our group reported new evidence showing that prenylated DIRAS3 interacts directly with RAS at the inner leaflet of the plasma membrane.[8] At the plasma membrane, the DIRAS3 α_5 helix can engage the RAS α_5 helical dimer interface to prevent RAS clustering and inhibit Raf dimerization and phosphorylation. This process requires plasma membrane anchoring of DIRAS3 through its CAAX box as well as an intact NTE. While the mechanism of binding of the DIRAS3 C-terminus to the plasma membrane by prenylation, which is similar to many other small GTPases, is well defined, the mechanism(s) by which the unique NTE of DIRAS3 associates with the cell membrane and mediates suppressor function is not well understood.

Membrane lipids play important roles in the signal transduction at the cell surface. In particular, phosphatidylinositol-3,4,5-trisphosphate (PIP_3) is a highly negatively charged phospholipid[9] and can interact directly and selectively with protein modules that specifically recognize their phosphorylated inositol headgroups. In doing so, phosphoinositides, such as PIP_3, promote multiple effector kinase pathways on the plasma membrane and participate in the regulation of survival and growth of normal and cancer cells.[10,11] Phosphatidylinositol 3-kinase (PI3K) catalyzes the production of PIP_3 by phosphorylating phosphatidylinositol-4, 5-bisphosphate (PIP_2). Many lipid-anchored small GTPases (e.g., Rho, Rac, Arf) associate with phosphoinositides with high specificities, providing membrane anchoring at sites of signaling.[12] Despite sharing extensive sequence homology with DIRAS3, KRAS preferentially binds with membrane phosphatidylserine (PS), the most abundant anionic phospholipid in the plasma membrane.[13] The select sorting of PS is critical to the function and pathology of KRAS. To understand the

[1]Department of Experimental Therapeutics, University of Texas MD Anderson Cancer Center, Houston, TX 77054, USA
[2]Department of Biochemistry and Molecular Biology, Baylor College of Medicine, Houston, TX 77030, USA
[3]Department of Cancer Systems Imaging, University of Texas MD Anderson Cancer Center, Houston, TX 77030, USA
[4]Department of Integrative Biology and Pharmacology, McGovern Medical School, University of Texas Health Science Center, Houston, TX 77030, USA
[5]These authors contributed equally
[6]Lead contact
*Correspondence: zlu@mdanderson.org (Z.L.), rbast@mdanderson.org (R.C.B.)
https://doi.org/10.1016/j.isci.2023.108151

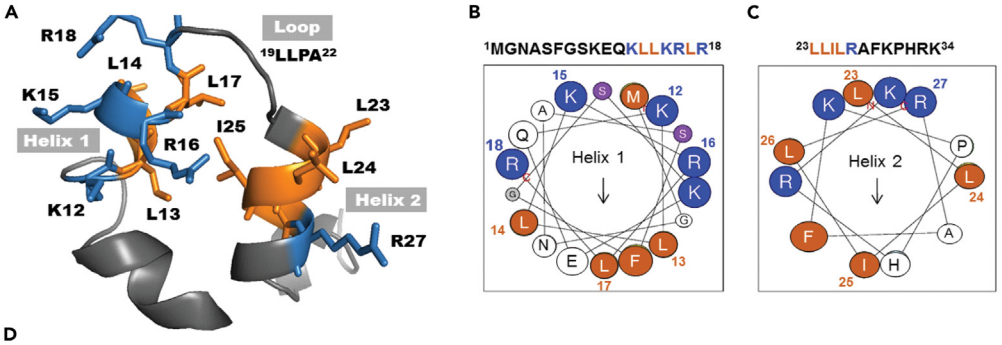

D

Name	Description	Sequence	MW (Da)
NTE_{wt}	NTE wild-type sequence 1-34	MGNASFGSKEQKLLKRLRLLPALLILRAFKPHRK	3931
NTE_{7LI}	Hydrophobic L&I to S&Q (7 aa)	MGNASFGSKEQKSSKRSRLLPASSQSRAFKPHRK	3790
NTE_{5KR}	Basic K&R to Q (5 aa)	MGNASFGSKEQQLLQQLQLLPALLILQAFKPHRK	3847
$NTE_{7LI+5KR}$	Combined hydrophobic & basic	MGNASFGSKEQQSSQQSQLLPASSQSQAFKPHRK	3706
NTE_{G2A}	Myristoyl site mutation	MANASFGSKEQKLLKRLRLLPALLILRAFKPHRK	3945
NTE_{3R}	Cancer mutations	MGNASFGSKEQKLLKWLQLLPALLILHAFKPHRK	3914
NTE_{scr}	Scrambled	MGLNASFLKLESRKPLAQKPALFIRLRGKLHRKL	3931
NTE_{2-11}	Partial helix 1	GNASFGSKEQ(SGG~)	1394
NTE_{12-29}	shorter helix-loop-helix	KLLKRLRLLPALLILRAF(SGG~)	2386
NTE_{2-11}-biotin	NTE_{2-11} biotin fusion	GNASFGSKEQ(SGG~PEG3-biotin)	1839
NTE_{12-29}-biotin	NTE_{12-29} biotin fusion	KLLKRLRLLPALLILRAF(SGG~PEG3-biotin)	2830
NTE_{wt}-biotin	Wild type NTE biotin fusion	MGNASFGSKEQKLLKRLRLLPALLILRAFKPHRK(biotin)	4175

Figure 1. DIRAS3 NTE predicted structure and synthetic peptides

(A) A structural model generated by Phyre2 shows that the 34 amino acids in the N-terminal region of DIRAS3 contains a basic-helix-loop-helix structural motif composed of two helices and a short loop region.

(B and C) Helix wheel presentations of amphipathic helix 1 and helix 2 with the rotated helix by placing its hydrophobic face downward. (HeliQuest, https://heliquest.ipmc.cnrs.fr/).[27]

(D) A panel of synthetic peptides for DIRAS3 NTE with wild-type and mutated sequences. See also Figures S2A, S2B, and S3C. The altered amino acids are colored, and hydrophobic loop region is underlined. Color coding for residues: blue for basic, brown for hydrophobic, green for polar.

underlying mechanism(s) of the DIRAS3 NTE that facilitate membrane binding and enable DIRAS3 function as a tumor suppressor, we characterized the structure and biochemical properties of the DIRAS3 N-terminal extension.

RESULTS

The N-terminal extension of DIRAS3 contains a helix-turn-helix motif with amphipathic properties

When we performed a BLAST search on the NTE sequence, we did not find any sequence homologous to known lipid-binding proteins. To determine how the N-terminal segment of DIRAS3 interacted with the plasma membrane, we analyzed the secondary structure of the NTE of DIRAS3. Our molecular modeling predicted a helix-loop-helix structure for the DIRAS3 NTE (residues 1–34), with numerous basic and hydrophobic residues concentrated in the region of amino acids 12–29 (Figure 1A). Both helix 1 and helix 2 have amphipathic feature (Figures 1B and 1C), while the loop region is mainly composed of hydrophobic residues. To elucidate the structure-function relationship of the N-terminal extension region, we generated a panel of NTE variants, including stretch mutations, point mutations, sequence rearrangements, and truncations (Figure 1D). To test whether the clustered hydrophobic and positively charged residues are required to form an amphipathic helix and to bind lipids, we designed a set of mutant peptides: hydrophobic residues leucine (L) and isoleucine (I) and charged residues lysine (K) and arginine (R) were replaced with serine or glutamine. NTE_{7LI} lacks the cluster of hydrophobic residues (6 leucine and 1 isoleucine), NTE_{5KR} lacks the cluster of positively charged residues (2 lysine and 3 arginine), and $NTE_{7LI+5KR}$ lacks both clusters (combined mutations of NTE_{7LI} and NTE_{5KR}). It has been proposed that NTE region of DIRAS3 has a specific site for lipid modification,[14,15] so the mutation of the glycine myristoylation site (G2A) was also included as NTE_{G2A}. From a survey of BioMuta single-nucleotide variation and disease association database[16] for amino acid mutations in the NTE region of DIRAS3 (Figure S2A), a mutant peptide NTE_{3R} was generated using mutations found in uterine cancer (Figure S2B). Using these synthetic peptides (Figure 1D), we applied biochemical/biophysical and computational methods to investigate NTE structure and its functional interactions.

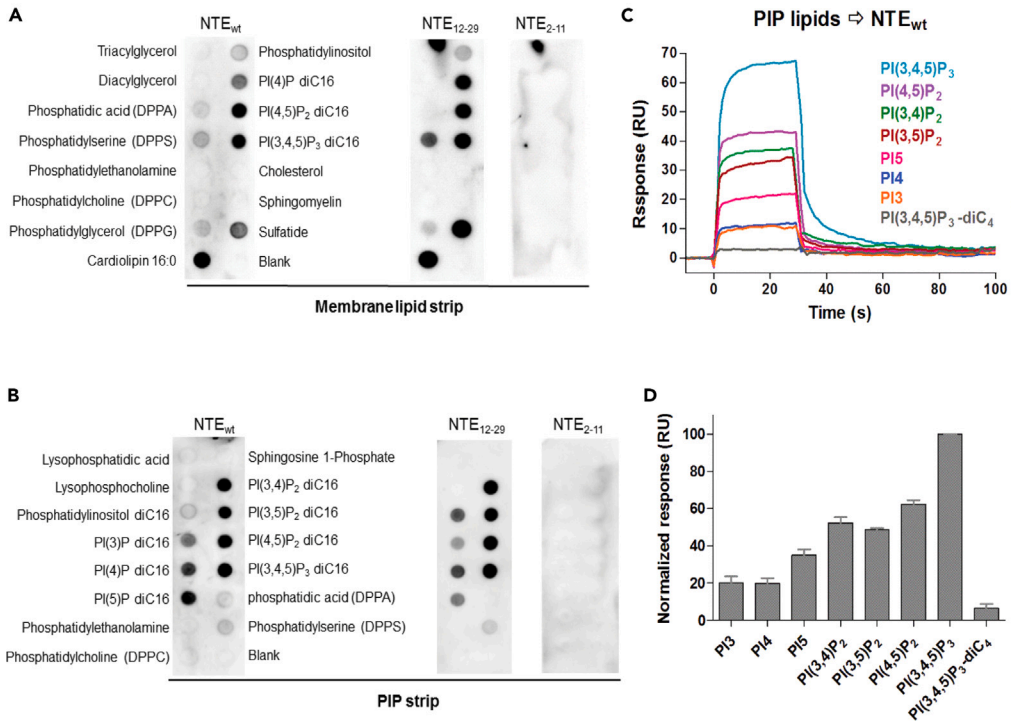

Figure 2. Lipid binding specificity of DIRAS3 NTE

(A and B) Peptide-lipid overlay assay. Biotin-conjugated peptide (1 μM of NTE$_{wt}$, 0.5 μM of NTE$_{12-29}$, and NTE$_{2-11}$) was added to the commercially available nitrocellulose membranes that were spotted with 100 pmol of different biologically important lipids found in cell membranes [long chain ($\geq C_{16}$) natural lipid or synthetic analogs] of (A) membrane lipid strip and all eight phosphoinositides lipids (B) PIP strip. Bound peptide was probed with HRP-conjugated streptavidin and detected with chemiluminescent HRP substrate. These experiments were repeated 3 times with similar results. See also Figure S3C.

(C and D) SPR experiment detected binding of synthetic PIP lipid (10 μM, all are diC$_8$ chain unless specified) over NTE$_{wt}$-biotin surface (~500 RU with MW of 4175 Da). Binding response (at 20 s) for each lipid (MW of 980 to 732 Da) was normalized and compared (n = 3). See also Figures S4E and S4F. *PI(3)P*, phosphatidylinositol (3)-phosphate; *S1P*, *PI(3,4)P$_2$*, phosphatidylinositol (3,4)-bisphosphate; *PI(3,4,5)P$_3$*, phosphatidylinositol (3,4,5)-trisphosphate.

The DIRAS3 NTE has affinity for anionic lipids, preferentially binding multivalent PIP$_3$ and PIP$_2$

As the amphipathic α-helix of the DIRAS3 NTE is well suited for lipid binding, we examined its interaction with natural lipids using membrane lipid strips. We found that NTE$_{wt}$ bound directly and preferentially to anionic lipids (ranked by estimated spot intensity reflecting the amount of peptide bound) ranging from cardiolipin (CL), phosphatidylinositol 3,4,5-trisphosphate (PI3,4,5P$_3$), phosphatidylinositol 4,5-bisphosphate (PI4,5P$_2$), phosphatidylinositol 4-phosphate (PI$_4$P), sulfatide (SULF) to phosphatidylserine (PS), with weak binding to phosphatidylglycerol (PG) and phosphatidic acid (PA) (Figure 2A). Fragment NTE$_{12-29}$ that contains a shorter helix-loop-helix motif showed the same lipid-binding pattern, but binding was not observed with the partial helix 1 NTE$_{2-11}$. A PI strip with all eight phosphoinositide lipids was also tested (Figure 2B). Both NTE$_{wt}$ and its structural fragment NTE$_{12-29}$ interacted with phosphatidylinositols, with stronger binding to the bis- and tris-phosphate forms. Data from both lipid dot blot assays indicated that NTE$_{wt}$ and its structural motif segment NTE$_{12-29}$ had the same lipid binding specificity. We further confirmed the interaction between the NTE peptide and PI lipids using a surface plasmon resonance binding assay (Figures 2C and 2D). The NTE-PI interaction did not appear to be a simple electrostatic attraction but required the coordinated effects of electrostatic (head group) and hydrophobic (acyl chain) interactions between the two molecules, in that PIP$_3$ with a shorter acyl chain (PI3,4,5P$_3$-diC$_4$) did not bind to NTE.

NTE recognizes PIP$_3$ and PIP$_2$ with rapid binding kinetics and high affinity

In a detailed analysis of the interaction with surface plasmon resonance (SPR), we found that the NTE$_{wt}$ bound strongly to PIP$_3$ with average K_D^{app} value of 0.68 μM ± 0.05 (standard deviation from n = 3). In contrast, the shorter helix-loop-helix segment (NTE$_{12-29}$) showed weak interaction, while the partial helix 1 (NTE$_{2-11}$) did not recognize PIP$_3$ (Figures 3A–3C). While the sensorgrams in Figure 2C were obtained by flowing lipid over immobilized peptide, the sensorgrams in Figures 3 and 4 were obtained by immobilizing the lipid and flowing over the unmodified peptide. Our observation of saturable, high-affinity binding in both experimental modes suggests a defined binding interaction between peptide and lipid rather than a non-saturable surface effect. Based on the SPR measurements, the binding affinity between NTE and PIP$_2$ (K_D^{app} = 0.73 μM ± 0.26, average with SD from n = 3) (Figure 3D) was similar to that of NTE-PIP$_3$. PIP$_2$ has less charge than PIP$_3$ and thus a weaker electrostatic interaction with the NTE was predicted. However, this difference could not be distinguished from SPR experiments,

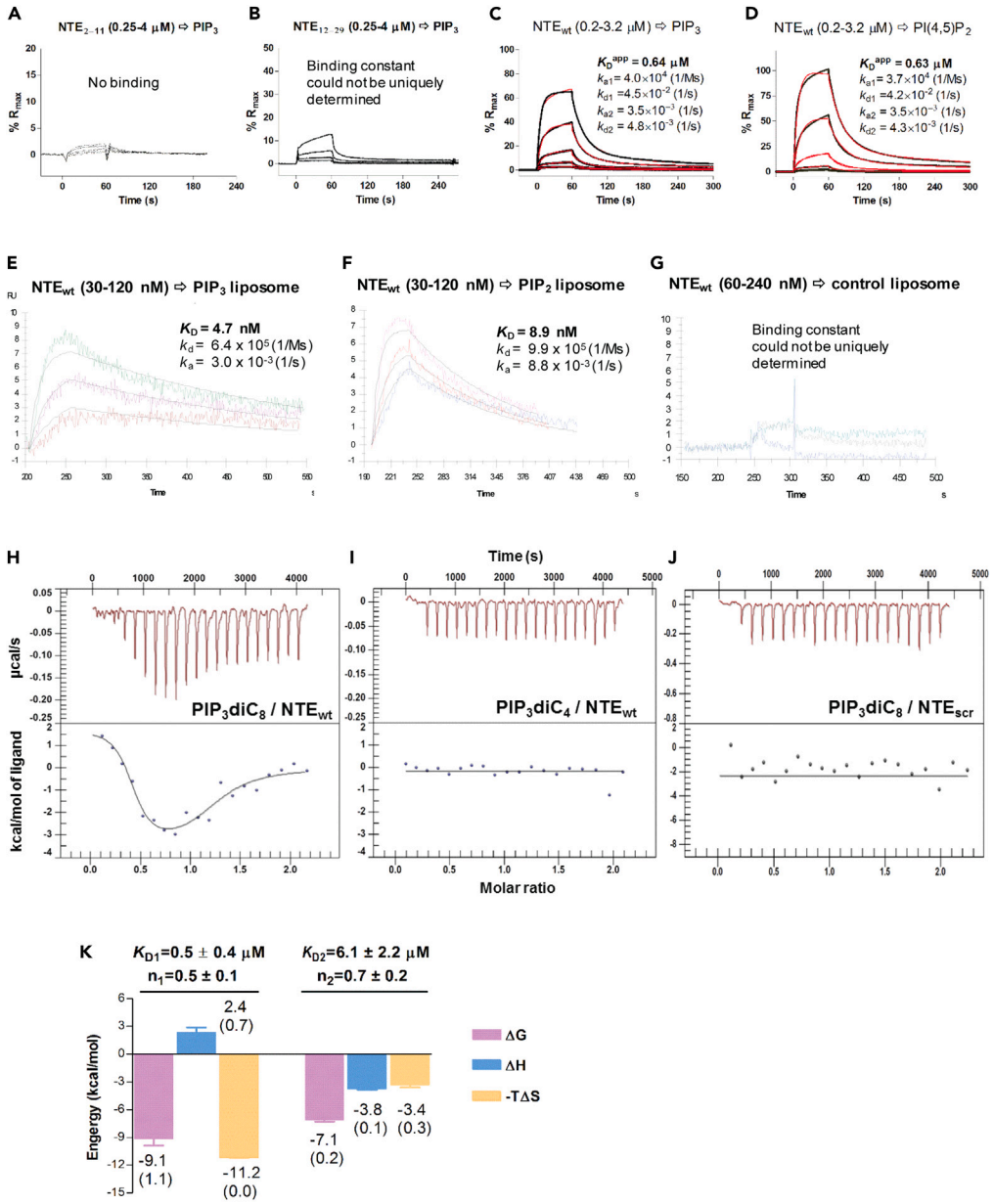

Figure 3. Biophysical analysis of the interactions of DIRAS3 NTE peptides with PIP_3 and PIP_2

(A–D) Representative SPR experiment for binding analysis on a $PIP_{3/2}diC_8$ lipid sensor (biotin-tethered): Peptide solution (2x or 3x dilution in buffer: 20 mM Tris, pH7.5, 150 mM NaCl, 0.02% Tween 20) of indicated concentration of (A) NTE_{2-11}, (B) NTE_{12-29}, and (C and D) NTE_{wt} at the concentrations indicated were injected onto PI-biotin (reference surface), $PI(3,4,5)P_3$-biotin or $PI(4,5)P_2$-biotin (~200 RU, captured by streptavidin immobilized on a Biacore sensor chip surface). SPR sensorgrams (shown in black) were fitted to a two-state binding model (in red), and the derived kinetic rate constants for the binding are listed. See also Figures S3A and S3B.

(E–G) SPR measurement of NTE_{wt} binding to surface tethered liposomes (~1500 RU for PIP_2 liposome, ~1700 RU for PIP_3 liposome, and ~1100 RU for control liposome). The NTE_{wt} bound sensorgram were fitted to a 1:1 binding model (in black) to obtain binding constants ($K_D = k_d/k_a$).

(H–K) ITC analysis of the binding reaction. (H) Blank-subtracted ITC data for the titration of PIP_3diC_8 (500 μM) onto NTE_{wt} peptide (78 μM) showing the thermogram (upper panel) and binding isotherm (lower panel) of integrated data point (black circles) fitted to a multiple-site model (black line, best fit model) using NanoAnalyze Data Analysis software to obtain thermodynamic parameters.

(I–J) Blank-subtracted ITC data for the titration of PIP_3diC_4 or PIP_3diC_8 (500 μM) onto NTE_{wt} or NTE_{scr} peptide (78 μM). No binding enthalpy can be detected, indicated by scattered data points around a fitted straight line. (K) Binding signatures plotted for thermodynamic parameters of the PIP_3diC_8–NTE_{wt} interaction. The average values (from two independent experiments, standard deviation in parentheses) of standard free energy (ΔG), binding enthalpy (ΔH), and entropy contribution (-TΔS) are shown for the binding of PIP_3 to site 1 and 2 on NTE_{wt}. The stoichiometry of binding (n), and apparent equilibrium-dissociation constant (K_D) are also listed.

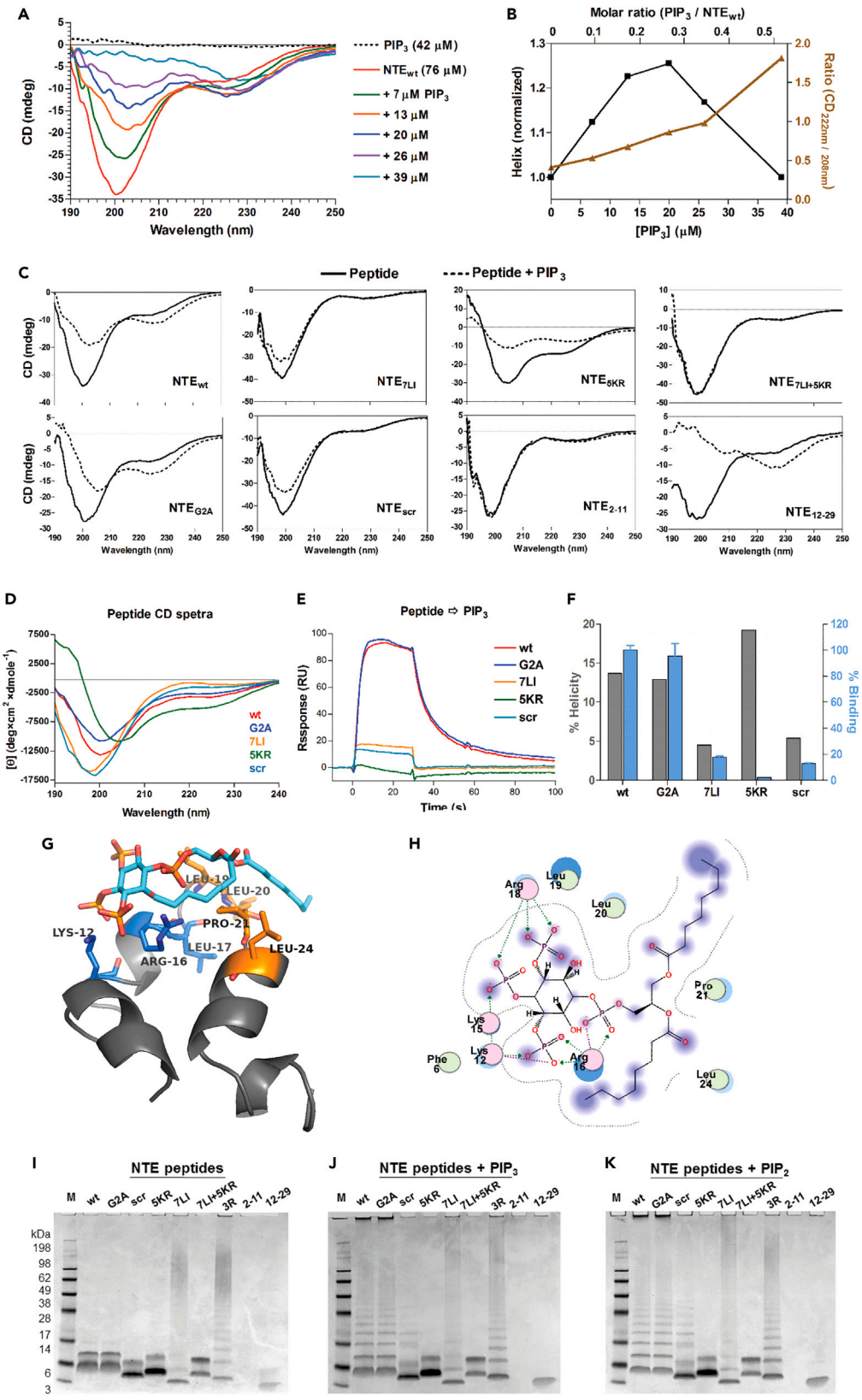
A
CD (mdeg)
Wavelength (nm)
PIP3 (42 μM)
NTEwt (76 μM)
+ 7 μM PIP3
+ 13 μM
+ 20 μM
+ 26 μM
+ 39 μM
B
Molar ratio (PIP3 / NTEwt)
Helix (normalized)
Ratio (CD222nm / 208nm)
[PIP3] (μM)
C
Peptide
Peptide + PIP3
NTEwt
NTE7LI
NTE5KR
NTE7LI+5KR
NTEG2A
NTEscr
NTE2-11
NTE12-29
D
Peptide CD spetra
[θ] (deg×cm2×dmole-1)
wt
G2A
7LI
5KR
scr
E
Peptide ⇨ PIP3
Rsponse (RU)
Time (s)
F
% Helicity
% Binding
G
LEU-10
LEU-20
PRO-21
LYS-12
LEU-17
LEU-24
ARG-16
H
Arg 18
Leu 19
Leu 20
Pro 21
Lys 15
Lys 12
Arg 16
Phe 6
Leu 24
I
NTE peptides
J
NTE peptides + PIP3
K
NTE peptides + PIP2
M
wt
G2A
scr
5KR
7LI
7LI+5KR
3R
2-11
12-29
kDa
198
98
62
49
38
28
17
14
6
3

Figure 4. Structural changes of NTE induced by PIP_3

(A–C) Secondary structure change was monitored by CD spectroscopy: (A) CD spectra are shown for NTE-WT peptide (0.3 mg mL^{-1}, 76 μM) in the absence or presence of PIP_3 (by titrating 1 μL of 2 mM PIP_3 into 300 μL of peptide, each final concentration is indicated). (B) The normalized helix (data point and line are in black) and the ratio of CD signal at 222 nm/208 nm (in brown, for evaluation of higher order structure) as a function of PIP_3 concentration are plotted. Molar ratio of PIP_3/NTE_{wt} is listed on the top. (C) CD spectra of NTE peptides (0.3 mg mL^{-1}) in the absence (solid line) or presence (dashed line) of PIP_3 (13 μM, final concentration).

(D–F) Correlation of NTE structure with its ligand-binding activity. (D) Overlay of CD spectra for NTE peptides (0.3 mg mL^{-1}). (E) Overlay of the SPR sensorgrams for binding of each peptide (1 μM) onto the streptavidin tethered PIP_3-biotin surface. (F) Comparison of the helicity of each peptde from (D) with their respective PIP_3-binding response (RU at 20 s time point) from (E).

(G and H) Computational analysis of the docked structure of PIP_3 binding to the WT DIRAS3 NTE.

(I–K) Multimerization of NTE was visualized by Coomassie staining of SDS-PAGE gel after glutaraldehyde cross-linking of NTE peptide (4 μg per lane) in the absence (I) and presence of PIP_3 (J) and PIP_2 (K). Peptide $NTE_{2\text{-}11}$ is not retained in the gel due to its small size (1394 Da). See also Figures S2C and S4.

which measured the overall binding, as NTE interacted with lipid through a combination of electrostatic and hydrophobic interactions. It also implies that hydrophobic interaction is much stronger than nonspecific electrostatic interaction for stable association of NTE with lipids. The electrostatic attraction seemed to be playing a crucial role for the recognition between NTE and PIP_3/PIP_2, as weaker bindings (K_D^{app} = 4.1 μM and 4.4 μM, respectively) were observed when the ionic strength of buffer was increased (Figures S3A and S3B). More importantly, in a similar SPR setup (Figures 3E–3G), PIP_3- or PIP_2- containing liposomes were specifically recognized by NTE_{wt} with even higher affinities (K_D values of 4.7 nM and 8.9 nM, respectively). The polymerized liposomes, containing 5% phosphoinositide, were tethered to the streptavidin chip via 1% biotin-PE incorporated. When the PIP_3 and PIP_2 headgroups are oriented on curvature surface in liposomes, more than 10-fold faster associations (6.4×10^5 vs. 4.0×10^4 1/Ms for PIP_3, and 9.9×10^5 vs. 3.7×10^4 1/Ms PIP_2) were observed, compared to the flat surface of biotin-PIP_3 and -PIP_2 (Figures 3C and 3D). The determined high affinity for the interaction, with rapid recognition kinetics, correlated well with the low levels of PIP_2 and PIP_3 in the dynamic plasma membrane and low expression of DIRAS3 in cancer cells.

To characterize the interaction further, we measured the binding energies of *NTE_{wt}*-PIP3 *in vitro* using isothermal titration calorimetry (ITC). Our analysis suggested that NTE_{wt}-PIP_3diC_8 binding was spontaneous with a small but detectable enthalpy change (Figure 3H). There was no detectable heat of binding reaction for NTE_{wt}-PIP_3diC_4 (Figure 3I) and NTE_{scr}-PIP_3diC_8 (Figure 3J). The "U" shaped binding isotherm indicated a complex interaction, which could be described by a two-site model with positive cooperativity and the ratio of binding at PIP_3:NTE = 1:2 (Figures 3H and 3K). The site 1 binding event (molar ratio 0 to ~0.7) had unfavorable enthalpy (ΔH = 2.4 kcal/mol ±0.7) due to structural rearrangement upon lipid binding (observed in CD experiments, Figures 4A and 4B) and weak electrostatic interaction, but high affinity (K_{D1} = 0.5 μM ± 0.4) due to a favorable entropic contribution (-TΔS = −11.2 kcal/mol ±0.0) and strong hydrophobic interactions. Compared to the first binding event, the second binding (molar ratio 0.7 to 2) was weaker (K_{D2} = 6.1 μM ± 2.2) and had different energetics, a favorable enthalpy (ΔH = −3.8 kcal/mol ±0.1) but smaller entropy (-TΔS = −3.4 kcal/mol ±0.3). This may be the result of multiple self-association events when more lipids were titrated in. When the Hill equation (Hill = 2/(1+((K_{D1}/(2*K_{D2}))^(1/2)) was applied to examine whether the two binding functions (lipid recognition and self-association) are dependent, the value of n(Hill), 1.7 ± 0.1, was greater than 1, consistent with cooperativity between two binding events. The site 1 binding molar ratio of 1:2 ($n_1 \approx 0.5$) suggests that one PIP_3 molecule binds two NTE_{wt} peptides. This lipid recognition has a dissociation constant (K_{D1}) value of 0.5 μM, comparable with that obtained by SPR (Figure 3C, K_D^{app} = 0.64 μM) using a simplified 2-state 1:1 binding model, suggesting each peptide has similar binding affinity.

PIP_3 binding induces structural change in the NTE

Using circular dichroism (CD) spectroscopy, we estimated that the NTE_{wt} peptide in solution is mainly random coil structure but contains a small amount of α-helical conformation. This mixed structure is demonstrated by the absence of a positive peak in the 190–200 nm region, and the presence of major negative peak at 200 nm and a small negative peak at 225 nm in the CD spectrum (Figure 4A). To understand the relationship between the structure and lipid-binding activities of NTE, we monitored the changes of peptide secondary structure upon addition of PIP_3. The analysis of the CD spectrum, using the CONTIN-LL and CDSSTR algorithms provided by DICHROWEB, indicated that NTE_{wt} contains a small amount of helix (estimated ~14%). While PIP_3 did not have any CD signal, adding PIP_3 resulted in a weakening of the negative peak at 200 nm and an enhanced the noticeably negative peak between 220 and 230 nm in the CD spectrum (Figure 4A), indicating a transition from a disordered structure to more helical structure (Figure 4B). This suggests a partially folded native conformation which is further stabilized through interaction with PIP_3, likely through the α-helical segment. With increased PIP_3, the peak intensity around 225 nm became dominant. As the (222/208) nm ratio is often used for tracking helical conformation (≤0.86 for isolated helices, ≥1 for higher order structures), a ratio plot was generated to track the effect of PIP_3 on conformational change of NTE_{wt} (Figure 4B). The shifting of the 222 nm peak to 230 nm indicated that some higher-order tertiary structure was formed presumably by PIP_3-induced peptide self-association. Interestingly, similar to ITC titration (Figure 3H), the structural change of the NTE_{wt} peptide was observed when PIP_3 was added at a ~0.1 molar ratio (or 1 PIP_3 per 10 NTE_{wt} molecule until the mixture became cloudy at >0.5 molar ratio, providing structural evidence for the thermodynamic characterization of the binding within this molar ratio range (Figure 3H).

To further elucidate mechanisms of NTE binding to PIP_3, we compared how different DIRAS3 NTE-related peptides bound to PIP_3. CD spectra in Figure 4C showed that NTE_{wt} and NTE_{G2A} had similar secondary structure transitions upon PIP_3 binding, but such transitions were not detected in NTE mutants aside from NTE_{5KR} (more helix). The partial helix 1 segment $NTE_{2\text{-}11}$ was largely disordered (~8% helical) and did not show CD change in the presence of PIP_3 (Figure 4C). The $NTE_{12\text{-}29}$ segment, a shorter helix-loop-helix, responded strongly to PIP_3

by shifting a mainly disordered (~11% helicity) structure in the absence of PIP_3 to a helical structure in the presence of PIP_3 (Figure 4C). Collectively, the CD data suggest there might be some enhanced helical content resulting from PIP_3 binding to the NTE_{wt} peptide but not to the scrambled or to (some of) the mutants, and the clustered positive charged and hydrophobic residues that promote amphipathic helix in NTE are crucial for PIP_3 binding.

Amphipathic mutations in the NTE functional motif affect its structure and ligand-binding activities

Molecular modeling suggested that mutation of the basic residues in aa12-29 of the NTE to glutamines should retain the helix-loop-helix structure (Figure S2C); however, side chains of key residues are predicted to point in directions opposite to those in the NTE wild-type structure. Three mutations observed in cancer, R16W, R16Q, and R27H (3R), are predicted to result in more linear structures than that of the WT NTE. However, further study is needed to determine whether this is the result of all three mutations together or if some combination of one or two mutations is enough to induce this structural change. A scrambled peptide, used as a negative control, did not display the helix-loop-helix structure of the NTE_{wt}.

Using CD spectroscopy and SPR binding, we further compared how mutations of DIRAS3 NTE peptide disrupted the structure and function of the amphipathic helix. As shown in Figure 4D, the stretch mutations within the amphipathic region (NTE_{7LI}, NTE_{5KR}, and $NTE_{7LI+5KR}$), as well as the scrambled NTE_{scr}, affected the peptide secondary structure with a noticeable change of CD signal intensity and a shift of CD minimum. The NTE_{G2A} mutant peptide, which has a single amino acid substitution outside the amphipathic region, did not show any significant change of the secondary structure compared to NTE_{wt}. Spectral analysis showed that NTE_{7LI}, $NTE_{7LI+5KR}$, and NTE_{scr} peptides contained the least helical content, whereas NTE_{G2A} had similar helicity to NTE_{wt} (Figure 4F). The NTE_{5KR} peptide shows the most change in the CD spectrum with positive signal in the 190–200 nm range along with minima at 220 nm and 208 nm suggesting helical content (Figures 4D and 4F). Comparing the binding of NTE mutants with PIP_3 using SPR, we found that mutations which alter the amphipathicity of the NTE structural motif dramatically reduce (by ~80%) the NTE binding to PIP_3 (Figures 4E and 4F). Interestingly, the NTE_{5KR} mutant, which was predicted to have a higher hydrophobicity due to the unchanged hydrophobic clustering and reduced net charge after the mutation, completely lost the ability to bind PIP_3, although this peptide has higher helicity, suggesting that electrostatic attraction is required for the interaction.

Computational docking analysis of PIP_3 and NTE_{wt} identified several key amino acids (Figure 4G) crucial to their interactions. In particular, K12, R16, and R18 formed hydrogen bonds and ionic interactions with the negative headgroups of PIP_3. Several hydrophobic residues were also predicted to interact with PIP_3, suggesting that both the basic and hydrophobic residues are necessary for the binding of PIP_3 to the NTE_{wt} (Figure 4H). Collectively, these data indicate that the structural and biochemical properties of the DIRAS3 NTE correlate with its ligand-binding function.

PIP_3 binding induces multimerization of NTE

Lipid binding-induced multimerization (tertiary structure change) of DIRAS3 NTE was visualized by Coomassie staining of cross-linked NTE peptides after SDS-PAGE electrophoresis (Figures 4I—4J). Glutaraldehyde cross-linking of peptide was carried out in the absence and presence of half molar amount of PIP_3 and PIP_2. In the absence of PIP_3 (Figure 4I), NTE wt and G2A peptides existed as monomers and dimers, while 7LI and 3R contained multimers. The predicted linear structure may explain the tendency of the cancer-mutant (3R) to multimerize even in the absence of PI; the linear structure (Figure S2C), with several of the hydrophobic residues on the same face of the peptide, may facilitate the formation of hydrophobic interactions, similar to how saturated hydrocarbon chains form hydrophobic interactions with each other more readily than do kinked, unsaturated hydrocarbon chains. It is worth noting that the slower migration of wt and G2A is likely due to binding of SDS micelles slowing the peptide migration. In the presence of half molar ratio of PIP_3 (Figure 4J), higher order multimers appear in the peptide of wt and G2A, consistent with CD observation (Figure 4B). Mutations in the NTE sequence, except the point mutation G2A, eliminate PIP_3 binding, so there is no binding-induced multimerization (Figure 4J). The effect of lipid-induced multimer formation is similar with PIP_2 (Figure 4K). Together with CD data, NTE has a mixed structure with a small portion of helical content that is enhanced upon lipid binding. The helix conformation has aggregation propensity due to unprotected hydrophobic patch that drives oligomerization.

Differential scanning fluorimetry (DSF) detected changes in NTE peptide folding induced by PIP_3 binding that could contribute to multimerization of the NTE-PIP_3 complex. Raw DSF measurement for the peptides showed that NTE_{3R} and NTE_{5KR} contain oligomers as indicated by high value of relative fluorescence unit (RFU) at 25°C, while all other peptides did not (RFU close to baseline) (Figure S4A). These data are consistent with the observation of the cross-linked multimer in Figure 4I. PIP_3-induced NTE peptide multimers are observed in NTE_{wt}, NTE_{5KR}, NET_{2GA}, and NTE_{scr} at 25°C–95°C (Figure S4B). Further analysis showed that PIP_3-induced NTE multimerization is concentration dependent in that more NTE oligomers (increased RFU value at 25°C) are induced in the presence of increased concentrations of PIP_3 and saturated at 1:1 molar ratio (Figure S4C). Higher-ordered multimers are more stable, indicated by higher T_m values (Figure S4D). The responsiveness of NTE to different PIP lipids (at 2:1 molar ratio) was compared in terms of formation of multimer (RFU value, Figure S4E) and oligomerized NTE-PI complex thermal stability (T_M value, Figure S4F). The results showed that among all the lipids tested, NTE aggregated in response to the binding of PIP_3, PIP_2, and phosphoinositol 5-monophosphate (PI_5P). This is consistent with the SPR binding data in Figure 2D. The stabilities (T_m) for the NTE_{wt}-lipid multimers are ranked as PIP_3 > $PI(4,5)P_2$ > PI_5P > $PI(3,4)P_2$ > $PI(3,5)P_2$. PIP_3-binding induced protein aggregation was also found in the DIRAS3 protein that includes the NTE region. As shown in Figure S4G, the NTE-deleted DIRAS protein (aa 35–225) did not show any change of RFU value in the presence of PIP_3, suggesting that the PIP_3-induced oligomerization of DIRAS3 (RFU increase) requires the presence of the NTE region of the protein. It is possible that DIRAS3 multimerization by PIP_3-binding is through NTE region.

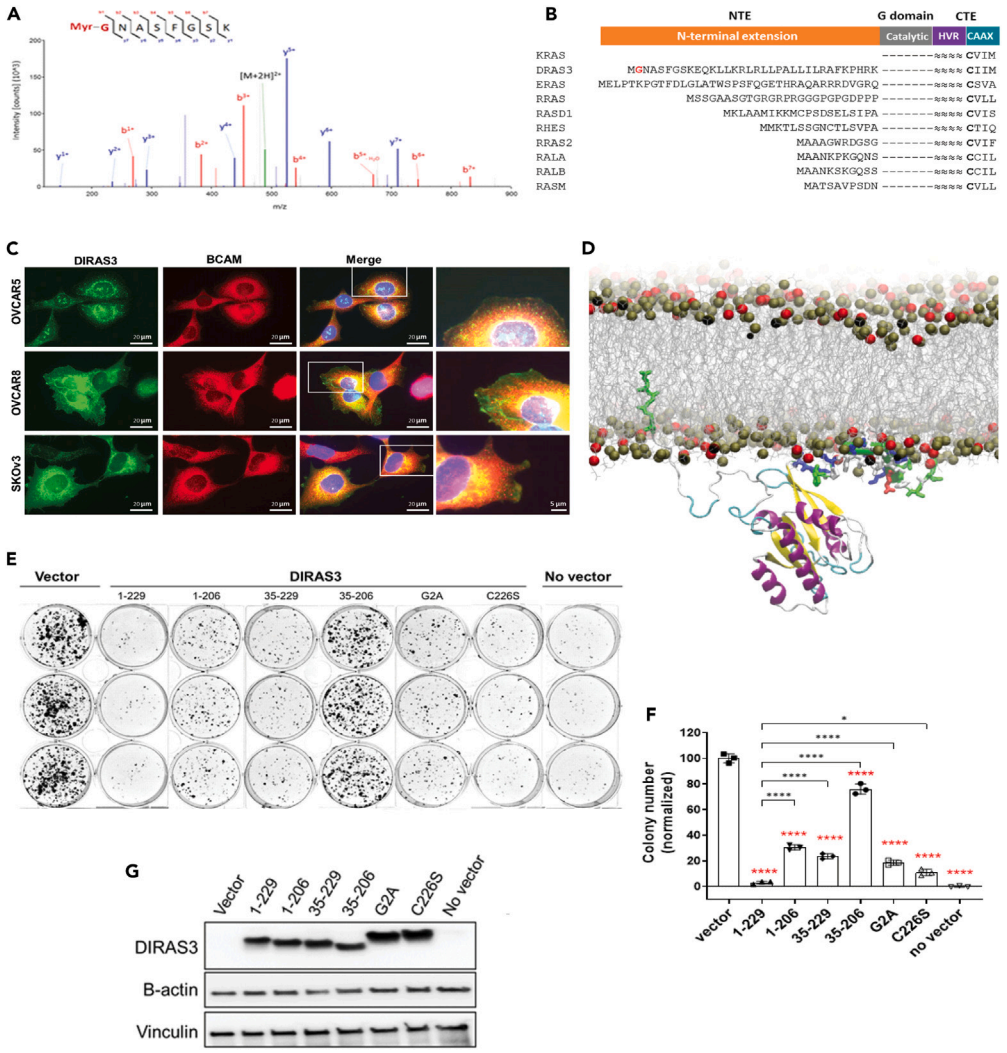

Figure 5. Requirement of N- and C-terminal lipid anchors for DIRAS3 function

(A) Direct evidence for lipid modification of DIRAS3 NTE. Mass spectrometry identified Myr-GNASFSGK peptide from an OVCAR8 ovarian cancer cell lysate with DOX-induced expression of DIRAS3 that was enriched with anti-DIRAS3 pAb, reduced/alkylated, trypsin-digested, and analyzed by LC-MS. MS/MS spectrum match indicates tryptic peptide containing residue G^2. See also Figure S5.

(B) N-terminal sequences of 12 RAS-related and CAAX-containing proteins are aligned with KRAS. DIRAS3 contains a 34 amino acid extension at the N-terminus of the G domain. The myristoylated glycine is highlighted in red. CTE (C-terminal extension) is membrane anchorage region composed of HVR (hypervariable region) and CAAX box. Cysteine residue (in bold) in the CAAX motif is the site for prenylation. See also Figure S6.

(C) DIRAS3 localizes at plasma membrane. OVCAR5, OVCAR8, and SKov3 ovarian cancer cells were stained with immunolabeled antibodies, recognizing DIRAS3 and BCAM, respectively. BCAM is a membrane protein.

(D) A model of DIRAS3 doubly anchored through NTE and CTE to a bilayer made up of phosphatidylcholine and 20% phosphatidylserine. See also Videos S1 and S2. The protein is shown in a cartoon representation with residues in contact with lipids indicated in licorice (blue = basic; red = acidic; green = polar; white = hydrophobic). Lipids are represented as gray lines with phosphorus atoms shown as brown balls for phosphatidylcholine and red for phosphatidylserine.

(E and F) Growth inhibition of DIRAS3 in HEK293 cells. Constructs for full-length (residues 1–229), NTE- and CTE-truncated DIRAS3 (residues 35–229 and 1–206, respectively), and point mutation of the myristoylation site (G2A) and prenylation site (C226S) were cloned in pcDNA3.1+ vector and transfected into HEK293. Colony formation were measured using a G418 selected clonogenic assay (E) and the colonies (>50 cells) were counted (F). Similar transfection efficiency for all the constructs was measured by western blot (G).

DIRAS3 NTE contains a myristoyl lipid tail

It has been speculated that the second glycine residue is a potential myristoylation site,[14] although it deviates from the N-myristoylation consensus motif $G^1X^2Z^3Z^4S^5Z^6$ after removal of first methionine (X = uncharged residue, Z = neutral residue, S = serine).[12] We used mass spectroscopy to test whether the NTE was myristoylated. Using OVCAR8 ovarian cancer cells that have stable expression of DIRAS3, a myristoylated peptide fragment was identified using mass spectrometry (Figure 5A). The same lipid-modified NTE fragment was also identified in

other cell lines (Figure S5). N-myrisoylation of glycine in DIRAS3 is unique among prenylated (CAAX motif containing) single-domain RAS family proteins (Figure 5B).

Membrane-anchored DIRAS3 by double-termini is required for its function

As previous studies indicated that both the N-terminus and the C-terminus of DIRAS3 are required for several suppressor functions including prevention of malignant transformation, growth inhibition, blocking motility, and inducing autophagy, we used AA-MD simulations to predict how the N-terminus and the C-terminus of DIRAS3 contributed to membrane binding. Our immunofluorescence staining demonstrated that DIRAS3 localizes at the plasma membrane (Figure 5C) in ovarian cancer cells, and modeling analysis showed that the full-length DIRAS3 protein adhered to the anionic lipid bilayer anchored by both the NTE and the C-terminal prenyl moiety, stabilizing the catalytic domain of DIRAS3 on the membrane by limiting its rotational and translational freedom. In addition, modeling analysis indicated that the catalytic domain, including helix α5, was completely solvent exposed (not occluded by the membrane) (Figures 5D and S6), suggesting that any part of the catalytic domain would be able to interact with partner proteins unimpeded. It is also likely that the doubly anchored DIRAS3 would facilitate α5-mediated interaction with KRAS dimer interface and inhibit KRAS clustering and signaling at the membrane surface.

To further confirm both the DIRAS3 NTE and the C-terminal prenyl moiety DIRAS3 are required for its inhibitory function, wild-type DIRAS3 and different DIRAS3 mutants were transfected into human embryonic kidney 293 cells. Transfected cells were selected with G418 and colonies were grown and counted. Wild-type DIRAS3(1–229) suppressed clonogenic growth, whereas deletion of the N-terminal (35–229), C-terminal (1–206), both N- and C- terminal (35–206), mutation of the glycine myristoylation site (G2A) or the CAAX box prenylation site (C226S) markedly reduced inhibition of clonogenic growth (Figures 5E and 5F), consistent with a requirement for double anchoring of DIRAS3 to the inner surface of the cell surface membrane to suppress tumor growth. Data in Figures 4C–4F show that the NTE_{wt} and G2A mutant structure and lipid binding are the same. However, the DIRAS3 function in the cell was inhibited by ~80% when G2A mutation is introduced (Figures 5E and 5F), suggesting that myristoylation may be responsible for anchoring and membrane localization of the NTE rather than the structure of the NTE itself.

DISCUSSION

Our study suggests that a myristoylated 34-amino acid N-terminal extension anchors the DIRAS3 protein to the inner surface of the plasma membrane after binding to $PI(3,4,5)P_3$ and $PI(4,5)P_2$. The prenylated C-terminus of DIRAS3, although lacking adjacent polybasic domain in the hypervariable region (Figure S6), also mediates binding of DIRAS3 to the inner surface of the plasma membrane. Mutation of the myristoylation site or deletion of the CAAX box markedly reduces the ability of DIRAS3 to suppress clonogenic cell growth, supporting the model that DIRAS3 must be doubly anchored at both the N-terminal and C-terminus for optimal function. Many reports have shown that proteins with N-terminal amphipathic helices interact with phospholipids and promote localization on the inner surface of the cell surface membrane.[13] In addition, some N-terminal domains are anchored by lipidation.[14] Our previous studies indicated that both the N-terminus and the C-terminus of DIRAS3 are required for several suppressor functions including prevention of malignant transformation, growth inhibition, blocking motility, and inducing autophagy.

Small guanosine triphosphatases (GTPases) from the RAS, Rho, Arf, and Rab subfamilies often exert their role at the plasma membrane where they control diverse signaling, cytoskeletal, and transport processes.[17–19] The membrane-targeting motifs of the small GTPases typically possess several classic features: a polybasic region containing a stretch of positively charged amino acids, and a hydrophobic region containing lipid anchors and/or hydrophobic amino acids. The lipid anchors can be conjugated to the N-terminus (myristoyl) and/or to the C-terminus (palmitoyl, farnesyl, or geranylgeranyl). These structural features provide intricate specificities for sorting of plasma membrane lipids for both headgroups and acyl chains. As DIRAS3 regulates the PI3K signaling pathway,[5] strong binding of the DIRAS3 to $PI(4,5)P_2$ and $PI(3,4,5)P_3$ suggests that DIRAS3 might be closely associated with PI3K, forming a binding platform that inhibits PI3K/AKT signaling by blocking the binding of the AKT PH domain to PIP_3.

RAS proteins must localize to the plasma membrane for biological function. The signal transduction activity of RAS proteins can be altered by both cell membrane lipids and by their own lipid modifications. Members of the RAS family contain a highly conserved G domain and a C-terminal hypervariable region (HVR) that is isoprenylated at the C-terminus for association with the plasma membrane.[20–22] The nature of lipidation is believed to contribute to functional specialization.[23] For example, all H-, N-, and K-RAS4B (simplified as KRAS) are farnesylated, but only N- and H-RAS are palmitoylated at one and 2 cysteine residues, respectively, whereas KRAS possesses a polybasic domain (PBD) containing 6 contiguous lysine residues upstream of the farnesylated cysteine.[22] These differences contribute to the observed lateral segregation of RAS isoforms to distinct lipid micro-domains on the plasma membrane and their functional diversity.[23,24] KRAS nanoclusters contain a high level of monovalent PS and PA but little multivalent PIP_2,[25,26] indicating more than just electrostatic interactions. Previously, we demonstrated that DIRAS3 interacts with KRAS on the PM, disrupts KRAS nanoclustering, and inhibits the KRAS-dependent MAPK signaling in ovarian and pancreatic cancers.[8] These data are consistent with our MD simulations where both the N-terminus and the C-terminus of DIRAS3 anchor to the anionic lipid bilayer and the α5 domain of DIRAS3 is free to bind to the α5 regions of KRAS (Figure 5D), preventing KRAS nanoclustering.[8] Moreover, these data align with our biological observation that deletion of the N-terminus or the C- terminus or mutation of the CAAX box markedly reduced inhibition of clonogenic growth (Figures 5E and 5F). Finally, our study also demonstrated that the DIRAS3 NTE peptide binds to PS (Figures 2A, 2B, and S3C), suggesting DIRAS3 may associate with KRAS in the PS-enriched KRAS nanoclusters to block KRAS signaling. Interestingly, when compared to KRAS, DIRAS3 protein lacks a PBD in its C-terminal HVR. Thus, DIRAS3 may sort

PS via a different mechanism than KRAS. It is likely that the NTE and the C-terminal HVR together provide the specificity for PS in the plasma membrane.

Analysis of the DIRAS3 protein sequence (Figure S6) indicates that, while the majority of RAS family members contain a glycine at position 12 (G^{12}), this functional residue is altered in DIRAS3 (A^{46}). This suggests that DIRAS3 does not act as a molecular switch.[2] Residues in switch II region, which are important for GTP hydrolysis (A^{59} and Q^{61} in KRAS), nucleotide exchange and effector interaction (G^{60} in KRAS), have also been altered in DIRAS3 (K^{93} and G^{95}, and S^{94}, respectively). These specific alternations in DIRAS3 have low intrinsic GTPase activity and a constitutively activated state (GTP-bound) in resting cells.[2]

In conclusion, our work supports a model where the tumor suppressor gene DIRAS3 is doubly anchored to the inner leaflet of the plasma membrane at both its N- and C-terminus, positioning the molecule to bind directly to KRAS and to disrupt KRAS dimers and clusters, inhibiting signaling from mutant RAS. Downregulation of DIRAS3, by multiple mechanisms, can contribute to the growth and motility of RAS-driven cancers.

Limitations of the study

This study explores the properties of the N-terminal peptide segment of DIRAS3, but its precise involvement and mechanism in membrane targeting need to be further studied using higher resolution techniques, biological membrane systems, and full-length protein where the NTE is in its structural context. For example, investigation of NTE peptides alone and in complex with lipids by NMR would provide additional information for structural and modeling work.

STAR★METHODS

Detailed methods are provided in the online version of this paper and include the following:

- KEY RESOURCES TABLE
- RESOURCE AVAILABILITY
  - Lead contact
  - Materials availability
  - Data and code availability
- EXPERIMENTAL MODEL AND STUDY PARTICIPANT DETAILS
- METHOD DETAILS
  - Peptide, lipid and liposome
  - Lipid dot blot assay
  - Surface plasmon resonance (SPR) analysis
  - Isothermal titration calorimetry
  - Circular dichroism spectroscopy
  - Thermal shift assay
  - Peptide crosslinking & SDS-PAGE
  - Mass spectrometry
  - Computational analysis and molecular docking
  - Molecular dynamic simulation
  - Immunofluorescence staining
  - Clonogenic assay
  - Immunoblotting
- QUANTIFICATION AND STATISTICAL ANALYSIS

SUPPLEMENTAL INFORMATION

Supplemental information can be found online at https://doi.org/10.1016/j.isci.2023.108151.

ACKNOWLEDGMENTS

The authors would like to thank members of the Bast laboratory for their suggestions and help. Instrument access was provided by Dr. Chun Li in the Department of Cancer Systems Imaging for the Biacore 3000 instrument, Drs. John Tainer and Roopa Thapar in the Departments of Molecular and Cellular Oncology and Cancer Biology for the CD instrument, and Drs. Jason B. Cross and Paul Leonard in the Institute for Applied Cancer Science, UT MD Anderson Cancer Center, for ITC instrument. This work was supported by R01 CA266187 (RC Bast and Z Lu PIs) from the National Cancer Institute, Department of Health and Human Services, and a CPRIT IIRA (RP200166) (S Millward and Z Lu PIs), Emerson collective cancer research fund, and Anne and Henry Zarrow Foundation, the Roberson Endowment and generous donations by Gaye Lynn and Stuart Zarrow. G.B. was supported by a CPRIT Training Award (RP210028), the HERA Ovarian Cancer Foundation, and the Mentored Investigator Award from the Ovarian Cancer Research Fund Alliance.

AUTHOR CONTRIBUTIONS

X.L., Z.L., and R.C.B. designed research; X.L., S.Y.J., L.W.F., G.B., W.M., S.Z., A.A.G., and Z.L. performed research and analyzed data; J.P.G., and S.W.M. contributed new reagents; X.L. drafted the paper; Z.L., R.C.B., S.Z., and Y.Z. revised the paper.

DECLARATION OF INTERESTS

The authors declare no competing interest.

Received: April 24, 2023
Revised: August 16, 2023
Accepted: October 3, 2023
Published: October 6, 2023

REFERENCES

1. Yu, Y., Xu, F., Peng, H., Fang, X., Zhao, S., Li, Y., Cuevas, B., Kuo, W.L., Gray, J.W., Siciliano, M., et al. (1999). NOEY2 (ARHI), an imprinted putative tumor suppressor gene in ovarian and breast carcinomas. Proc. Natl. Acad. Sci. USA *96*, 214–219. https://doi.org/10.1073/pnas.96.1.214.
2. Luo, R.Z., Fang, X., Marquez, R., Liu, S.Y., Mills, G.B., Liao, W.S.L., Yu, Y., and Bast, R.C. (2003). ARHI is a Ras-related small G-protein with a novel N-terminal extension that inhibits growth of ovarian and breast cancers. Oncogene *22*, 2897–2909. https://doi.org/10.1038/sj.onc.1206380.
3. Wang, L., Hoque, A., Luo, R.Z., Yuan, J., Lu, Z., Nishimoto, A., Liu, J., Sahin, A.A., Lippman, S.M., Bast, R.C., Jr., and Yu, Y. (2003). Loss of the expression of the tumor suppressor gene ARHI is associated with progression of breast cancer. Clin. Cancer Res. *9*, 3660–3666.
4. Bildik, G., Liang, X., Sutton, M.N., Bast, R.C., and Lu, Z. (2022). DIRAS3: An Imprinted tumor suppressor gene that regulates RAS and PI3K-driven cancer growth, motility, autophagy and tumor dormancy. Mol. Cancer Therapeut. *21*, 25–37. https://doi.org/10.1158/1535-7163.mct-21-0331.
5. Lu, Z., Luo, R.Z., Lu, Y., Zhang, X., Yu, Q., Khare, S., Kondo, S., Kondo, Y., Yu, Y., Mills, G.B., et al. (2008). The tumor suppressor gene ARHI regulates autophagy and tumor dormancy in human ovarian cancer cells. J. Clin. Invest. *118*, 3917–3929. https://doi.org/10.1172/JCI35512.
6. Badgwell, D.B., Lu, Z., Le, K., Gao, F., Yang, M., Suh, G.K., Bao, J.J., Das, P., Andreeff, M., Chen, W., et al. (2012). The tumor-suppressor gene ARHI (DIRAS3) suppresses ovarian cancer cell migration through inhibition of the Stat3 and FAK/Rho signaling pathways. Oncogene *31*, 68–79. https://doi.org/10.1038/onc.2011.213.
7. Lu, Z., Yang, H., Sutton, M.N., Yang, M., Clarke, C.H., Liao, W.S.L., and Bast, R.C., Jr. (2014). ARHI (DIRAS3) induces autophagy in ovarian cancer cells by downregulating the epidermal growth factor receptor, inhibiting PI3K and Ras/MAP signaling and activating the FOXo3a-mediated induction of Rab7. Cell Death Differ. *21*, 1275–1289. https://doi.org/10.1038/cdd.2014.48.
8. Sutton, M.N., Lu, Z., Li, Y.C., Zhou, Y., Huang, T., Reger, A.S., Hurwitz, A.M., Palzkill, T., Logsdon, C., Liang, X., et al. (2019). DIRAS3 (ARHI) Blocks RAS/MAPK Signaling by Binding Directly to RAS and Disrupting RAS Clusters. Cell Rep. *29*, 3448–3459.e6. https://doi.org/10.1016/j.celrep.2019.11.045.
9. Siess, K.M., and Leonard, T.A. (2019). Lipid-dependent Akt-ivity: where, when, and how. Biochem. Soc. Trans. *47*, 897–908. https://doi.org/10.1042/bst20190013.
10. Cantley, L.C. (2002). The phosphoinositide 3-kinase pathway. Science (New York, N.Y.) *296*, 1655–1657. https://doi.org/10.1126/science.296.5573.1655.
11. Osaki, M., Oshimura, M., and Ito, H. (2004). PI3K-Akt pathway: its functions and alterations in human cancer. Apoptosis *9*, 667–676. https://doi.org/10.1023/B:APPT.0000045801.15585.dd.
12. Johnson, D.R., Bhatnagar, R.S., Knoll, L.J., and Gordon, J.I. (1994). Genetic and biochemical studies of protein N-myristoylation. Annu. Rev. Biochem. *63*, 869–914. https://doi.org/10.1146/annurev.bi.63.070194.004253.
13. Giménez-Andrés, M., Čopič, A., and Antonny, B. (2018). The Many Faces of Amphipathic Helices. Biomolecules *8*, 45. https://doi.org/10.3390/biom8030045.
14. Jiang, H., Zhang, X., Chen, X., Aramsangtienchai, P., Tong, Z., and Lin, H. (2018). Protein Lipidation: Occurrence, Mechanisms, Biological Functions, and Enabling Technologies. Chem. Rev. *118*, 919–988. https://doi.org/10.1021/acs.chemrev.6b00750.
15. Colicelli, J. (2004). Human RAS superfamily proteins and related GTPases. Sci. STKE *2004*, RE13. https://doi.org/10.1126/stke.2502004re13.
16. Dingerdissen, H.M., Torcivia-Rodriguez, J., Hu, Y., Chang, T.C., Mazumder, R., and Kahsay, R. (2018). BioMuta and BioXpress: mutation and expression knowledgebases for cancer biomarker discovery. Nucleic Acids Res. *46*, D1128–D1136. https://doi.org/10.1093/nar/gkx907.
17. Fivaz, M., and Meyer, T. (2003). Specific localization and timing in neuronal signal transduction mediated by protein-lipid interactions. Neuron *40*, 319–330. https://doi.org/10.1016/s0896-6273(03)00634-2.
18. Teruel, M.N., and Meyer, T. (2000). Translocation and reversible localization of signaling proteins: a dynamic future for signal transduction. Cell *103*, 181–184. https://doi.org/10.1016/s0092-8674(00)00109-4.
19. Guan, J.L. (2004). Cell biology. Integrins, rafts, Rac, and Rho. Science (New York, N.Y.) *303*, 773–774. https://doi.org/10.1126/science.1094376.
20. Hancock, J.F., Magee, A.I., Childs, J.E., and Marshall, C.J. (1989). All ras proteins are polyisoprenylated but only some are palmitoylated. Cell *57*, 1167–1177. https://doi.org/10.1016/0092-8674(89)90054-8.
21. Wittinghofer, A., and Vetter, I.R. (2011). Structure-function relationships of the G domain, a canonical switch motif. Annu. Rev. Biochem. *80*, 943–971. https://doi.org/10.1146/annurev-biochem-062708-134043.
22. Cox, A.D., and Der, C.J. (2010). Ras history: The saga continues. Small GTPases *1*, 2–27. https://doi.org/10.4161/sgtp.1.1.12178.
23. Hancock, J.F. (2003). Ras proteins: different signals from different locations. Nat. Rev. Mol. Cell Biol. *4*, 373–384. https://doi.org/10.1038/nrm1105.
24. Weise, K., Kapoor, S., Denter, C., Nikolaus, J., Opitz, N., Koch, S., Triola, G., Herrmann, A., Waldmann, H., and Winter, R. (2011). Membrane-mediated induction and sorting of K-Ras microdomain signaling platforms. J. Am. Chem. Soc. *133*, 880–887. https://doi.org/10.1021/ja107532q.
25. Cho, K.J., van der Hoeven, D., Zhou, Y., Maekawa, M., Ma, X., Chen, W., Fairn, G.D., and Hancock, J.F. (2016). Inhibition of Acid Sphingomyelinase Depletes Cellular Phosphatidylserine and Mislocalizes K-Ras from the Plasma Membrane. Mol. Cell Biol. *36*, 363–374. https://doi.org/10.1128/MCB.00719-15.
26. Zhou, Y., Liang, H., Rodkey, T., Ariotti, N., Parton, R.G., and Hancock, J.F. (2014). Signal integration by lipid-mediated spatial cross talk between Ras nanoclusters. Mol. Cell Biol. *34*, 862–876. https://doi.org/10.1128/MCB.01227-13.
27. Gautier, R., Douguet, D., Antonny, B., and Drin, G. (2008). HELIQUEST: a web server to screen sequences with specific alpha-helical properties. Bioinformatics *24*, 2101–2102. https://doi.org/10.1093/bioinformatics/btn392.
28. Whitmore, L., and Wallace, B.A. (2008). Protein secondary structure analyses from circular dichroism spectroscopy: methods and reference databases. Biopolymers *89*, 392–400. https://doi.org/10.1002/bip.20853.
29. Kelley, L.A., Mezulis, S., Yates, C.M., Wass, M.N., and Sternberg, M.J.E. (2015). The Phyre2 web portal for protein modeling, prediction and analysis. Nat. Protoc. *10*, 845–858. https://doi.org/10.1038/nprot.2015.053.
30. Maupetit, J., Derreumaux, P., and Tuffery, P. (2009). PEP-FOLD: an online resource for de novo peptide structure prediction. Nucleic Acids Res. *37*, W498–W503. https://doi.org/10.1093/nar/gkp323.
31. Prakash, P., Litwin, D., Liang, H., Sarkar-Banerjee, S., Dolino, D., Zhou, Y.,

Hancock, J.F., Jayaraman, V., and Gorfe, A.A. (2019). Dynamics of Membrane-Bound G12V-KRAS from Simulations and Single-Molecule FRET in Native Nanodiscs. Biophys. J. *116*, 179–183. https://doi.org/10.1016/j.bpj.2018.12.011.

32. Prakash, P., Zhou, Y., Liang, H., Hancock, J.F., and Gorfe, A.A. (2016). Oncogenic K-Ras Binds to an Anionic Membrane in Two Distinct Orientations: A Molecular Dynamics Analysis. Biophys. J. *110*, 1125–1138. https://doi.org/10.1016/j.bpj.2016.01.019.

33. Gorfe, A.A., Hanzal-Bayer, M., Abankwa, D., Hancock, J.F., and McCammon, J.A. (2007). Structure and dynamics of the full-length lipid-modified H-Ras protein in a 1,2-dimyristoylglycero-3-phosphocholine bilayer. J. Med. Chem. *50*, 674–684. https://doi.org/10.1021/jm061053f.

STAR★METHODS

KEY RESOURCES TABLE

REAGENT or RESOURCE	SOURCE	IDENTIFIER
Antibodies		
DIRAS3 polyclonal	Robert Bast Lab	N/A
DIRAS3 (1D8 and 15E11) mouse monoclonal	Robert Bast Lab	N/A
β-actin	Cell Signaling	4970; RRID: AB_2223172
vinculin	Sigma	V9264; RRID: AB_10603627
BCAM	Santa Cruz	Sc-365191;RRID: AB_10709320
Chemicals, peptides, and recombinant proteins		
Synthetic phosphoinositide lipids and polymerized liposomes, see Figure S1	Echelon Biosciences	Catalog numbers are listed in Figure S1
Peptides for DIRAS3-NTE, see Figure 1D	Robert Bast Lab	N/A
Streptavidin-HRP	Thermo Fisher Scientific	21130; RRID: AB_11153518
SYPRO Orange	Sigma-Aldrich	S5692
Glutaraldehyde	Sigma-Aldrich	G7651
DIRAS3 full-length (aa 1–225) and NTE-truncated (aa 35–225)	This paper	N/A
Trypsin, Mass & Sequencing Grade	Gendepot	T9600
Critical commercial assays		
Membrane Lipid Strips	Echelon Biosciences	P-6002
PIP Strips	Echelon Biosciences	P-6001
ECL-enhanced chemiluminescence detection kit	Thermo Fisher Scientific	34580
SPR/biacore sensor chip SA	Cytiva	BR100032
Experimental models: Cell lines		
Human ovarian cancer: OVCAR8 (DIRAS3 inducible)	Robert Bast Lab	N/A
Human ovarian cancer: OVCAR5 (DIRAS3 inducible)	Robert Bast Lab	N/A
Human ovarian cancer: SKOv3 (DIRAS3 inducible)	Robert Bast Lab	N/A
Human ovarian cancer: HEY (DIRAS3 inducible)	Robert Bast Lab	N/A
Human: HEK293	ATCC	CRL-1573
Recombinant DNA		
pcDNA3.1(+) vector	Invitrogen	35–0484
Plasmids: pcDNA3.1(+)-DIRAS3 wt & mutants	Robert Bast Lab	N/A
Software and algorithms		
HeliQuest	Gautier et al.[27]	https://heliquest.ipmc.cnrs.fr/
BIAevaluation	GE Healthcare/Cytiva	Version 4.1
NanoAnalyze	TA Instruments	Version 3.10
DICHROWEB	Wittinghofer et al.21	http://dichroweb.cryst.bbk.ac.uk/html/home.shtml
Mascot Search Engine	Matrix Science	version 2.4
Phyre2	Kelley et al.[29]	http://www.sbg.bio.ic.ac.uk/phyre2
MOE	Chemical Computing Group (https://www.chemcomp.com/)	version 2019.0102
PyMOL	Schrodinger (https://pymol.org/2/)	Version 2.5.2

(*Continued on next page*)

Continued

REAGENT or RESOURCE	SOURCE	IDENTIFIER
PEPFOLD	Maupetit et al.[30]	http://bioserv.rpbs.univ-paris-diderot.fr/services/PEP-FOLD
Proteome Discoverer	Thermo Fisher	Version 2.1
GraphPad Prism	GraphPad Software	version 8.0
Other		
SPR biosensor Biacore 3000	GE Healthcare/Cytiva	https://www.cytivalifesciences.com/en/la/shop/protein-analysis/spr-label-free-analysis/
TA nano ITC	TA Instruments	https://www.tainstruments.com/products/microcalorimetry/isothermal-titration-calorimetry/
JASCO J-810 spectropolarimeter	JASCO Inc.	https://jascoinc.com/products/spectroscopy/circular-dichroism/
Nano HPLC	Thermo Fisher Scientific	nLC-1000
CFX Connect™ real-time PCR detection system	Bio-Rad	1855201
fatty acid-free BSA	EMD Millipore	126609
Slide-A-Lyzer Dialysis Cassettes 2 k mwco	Thermo Fisher Scientific	66205
NuPAGE 10% Bis-Tris gel	Thermo Fisher Scientific	NP0301
NuPAGE MES SDS Buffer Kit	Thermo Fisher Scientific	NP0060
Mass Spectrometer	Thermo Fisher Scientific	Orbitrap Fusion™ Lumos™ Tribrid™ Mass Spectrometer

RESOURCE AVAILABILITY

Lead contact

Further information and requests for resources should be directed to lead contact, Dr. Robert Bast (rbast@mdanderson.org).

Materials availability

This study did not generate new unique reagents.

Data and code availability

- This paper analyzes existing, publicly available data. These accession numbers for the datasets are listed in the key resources table. The software and algorithms used in this study are described in the method details section and the key resources table.
- Any additional information required to reanalyze the data reported in this paper is available from the lead contact upon request.

EXPERIMENTAL MODEL AND STUDY PARTICIPANT DETAILS

Tet-on inducible SKOv3-DIRAS3 cells were grown in McCoy's A medium, while OVCAR5-DIRAS3 and OVCAR8-DIRAS3 cell grown in RPMI medium. Medium was supplemented with 10% tet-system approved FBS, 200 μg/mL G418, and 0.12 μg/mL puromycin. DIRAS3 expression was induced by adding 1 μg/mL DOX to the culture medium. HEK293 human embryo kidney cells were grown in Dulbecco's modified Eagle's medium containing 10% fetal bovine serum.

METHOD DETAILS

Peptide, lipid and liposome

All 34-aa peptides were purchased from GenScript (GenScript USA Inc., Piscataway, NJ) using custom peptides synthesis services (>95% purity and standard TFA removal). Mass spectra were analyzed to ensure the quality of the peptide. Shorter peptides (>95% purity) were synthesized in our facility at MD Anderson. Synthetic phosphoinositide lipids and polymerized liposomes were purchased from Echelon Biosciences (Salt Lake City, UT). Their chemical structures are shown in Figure S1. All liposome solutions contained 1 mM total lipid. The average size of the liposome-like nanoparticles was approximately 200 nm. Phosphoinositide-containing PolyPIPosomes included 5% phosphoinositide (PIP_3 or PIP_2), 65% PC, 29% PE, and 1% biotin-PE. Control PolyPIPosomes included 70% PC, 29% PE, and 1% biotin-PE.

Lipid dot blot assay

Membrane Lipid Strips (P-6002; Echelon Biosciences, Salt Lake City, UT) and PIP Strips (P-6001; Echelon Biosciences, Salt Lake City, UT) were covered in blocking buffer with 3% fatty acid-free BSA (126609; EMD Millipore, Burlington, MA) in TBST [10 mM Tris, pH 7.5, 150 mM NaCl, and 0.1% Tween 20 (23336; Acros organics, Fair Lawn, NJ)] at room temperature for 1 h with gentle agitation. The strips were then incubated with 0.5 or 1 μM of biotinylated peptides at room temperature for 30 min. After washing three times in TBST (10–15 min for each wash), the strips were incubated with a 1:2000 dilution of streptavidin-HRP (21130; Thermo Scientific Pierce) in blocking buffer at room temperature for 30 min, followed by washing three times with TBST. Bound peptide-biotin were detected using ECL-enhanced chemiluminescence detection kit (SuperSignal West Pico PLUS, Thermo Fisher Scientific), then visualized with FluorChemE by 10–40 s exposure. Images were reversed to black/white and adjusted to achieve good contrast and brightness. All of the lipids used for lipid strips were long chain (≥C16) highly pure natural or synthetic analogs: *TG*, triacylglycerol; *DAG*, diacylglycerol; *PA*, phosphatidic acid; *PS*, phosphatidylserine; *PE*, phosphatidylethanolamine; *PC*, phosphatidylcholine; *PG*, phosphatidylglycerol; *CL*, cardiolipin; *PI*, phosphatidylinositol; *CHOL*, cholesterol; *SM*, sphingomyelin; *SULF*, sulfatide; *LPA*, lysophosphatidic acid; *LPC*, lysophosphocholine; *PI*, phosphatidylinositol; *PI(3)P*, phosphatidylinositol (3)-phosphate; *S1P*, sphingosine 1-phosphate; *PI(3,4)P$_2$*, phosphatidylinositol (3,4)-bisphosphate; *PI(3,4,5)P$_3$*, and phosphatidylinositol (3,4,5)-trisphosphate.

Surface plasmon resonance (SPR) analysis

Surface plasmon resonance-based binding experiments were carried out at 25°C using a Biacore 3000 optical biosensor (GE Healthcare/Biacore, Uppsala, Sweden) with a streptavidin-immobilized sensor chip (sensor chip SA, GE Healthcare). Synthetic peptides (Figure 1D) and lipid analogs (Echelon Biosciences, chemical information in Figure S1) were dissolved in Milli Q water to prepare a 1 mM stock solution. To capture biotin-conjugated ligand, a flow rate of 20 μL min^{-1} was used to inject the ligand (20–100 nM) until the desired density (~200 RU for lipid, and ~500 RU for peptide) was reached. The surface was then treated to remove loosely bound ligand by sequential injection of 1 M NaCl, 0.1% SDS, and 10 mM NaOH (30 s for each injection). A flow rate of 30 μL min^{-1} was used for all binding experiments. To regenerate the ligand surface, the bound analyte was removed with a 15-s injection of 0.1% SDS followed by 10 mM NaOH. The sensorgrams were shown in a format of "analyte ⇨ ligand," in that soluble analyte was injected onto a biotin-tethered ligand surface. All SPR responses were baseline and buffer corrected by subtracting the systematic noise from the corresponding reference surface: biotin-phosphatidylinositol (PI-biotin) was used as reference surface for ligands PIP$_3$-biotin and PIP$_2$-biotin. Streptavidin without ligand was used as reference surface for peptide-biotin.

For liposome binding SPR assays, biotin-labeled liposome (Echelon Biosciences, chemical information in Figure S1) solution was diluted 100-fold in HBS running buffer (20 mM HEPES at pH7.3, 150 mM NaCl) and injected onto the streptavidin flow cell at a flow rate of 10 μL min^{-1} until saturation. The liposome surface was then conditioned by three consecutive 30s injection of 5 mM NaOH at high flow rate (100 μL min^{-1}). NTE peptides were diluted into HBS running buffer containing 0.1 mg mL^{-1} fatty acid-free BSA and injected at 50 μL min^{-1} for the binding assay.

Theoretical maximum response for 1:1 binding (R_{max}) was calculated using Equation 1, where R_{immob} is the SPR response of the tethered ligand, MW_{sol} and MW_{immob} are molecular weight of soluble and immobilized molecule respectively.

$$R_{max} = (MW_{sol} / MW_{immob}) \times R_{immob} \quad \text{(Equation 1)}$$

For binding where conformational changes were involved, SPR response curves were globally fit to a predefined, two-state reaction model, where the association and dissociation rate constants (k_{a1}, k_{d1}) were for the binding state (A + B ↔ AB), and forward and backward rate constants (k_{a2}, k_{d2}) were for the conformational change state (AB ↔ AB*). This model describes 1:1 binding of analyte to immobilized ligand followed by a conformational change in the complex (BIAevaluation Software Handbook, edition 2004). It simply assumes that the only way AB* can dissociate to release free A is through prior conversion to the form AB. An apparent dissociation constant (K_D^{app}) was calculated from the kinetic parameters obtained from the curve fitting:

$$A + B \underset{k_{d1}}{\overset{k_{a1}}{\leftrightarrow}} AB \underset{k_{d2}}{\overset{k_{a2}}{\leftrightarrow}} AB* \quad \text{(Equation 2)}$$

$$K_D app = 1 / ((k_{a1} / k_{d1}) \times (1 + k_{a2} / k_{d2})) \quad \text{(Equation 3)}$$

Isothermal titration calorimetry

Experiments were performed using a TA nano ITC instrument (TA Instruments, New Castle, DE) at 25°C. Peptide stock solution was dialyzed in TBS buffer (25 mM Tris-HCl, pH 7.5, 150 mM NaCl) using Slide-A-Lyzer Dialysis Cassettes with 2k MWCO (ThermoFisher Scientific, 66205) at 4°C for 24 h with twice buffer changes. Lipid was dissolved in the final dialysis buffer. Titrations of PIP$_3$diC$_8$ or PIP$_3$diC$_4$ (500 μM) were performed in sample cells that contained NTE$_{wt}$ peptide (78 μM). Each titration began with a 0.4-μL injection followed by 2.5 μL injections. Each injection was spaced at 200-s intervals at a stirring speed of 300 rpm. Blank heat of dilution was measured by titrating the same PIP$_3$ into the buffer. Blank-subtracted ITC data were fitted using the multiple-site model using NanoAnalyze software (Version 3.10.0, TA Instruments).

Circular dichroism spectroscopy

Far-ultraviolet CD spectra were recorded at 25°C on a JASCO J-810 spectropolarimeter (JASCO Inc., Easton, MD) using a Suprasil quartz cuvette (Hellma GmbH) of 0.1 cm path-length. Measurements were taken between 190 and 250 nm at 2 nm intervals. The scan speed was set with a response time of 1 s and a step resolution of 0.2 nm. The results represent the average of five scans. All spectra were background-corrected by subtracting corresponding blank spectra without the peptide. Each peptide was resuspended in 10 mM potassium phosphate (pH 7.4) at 3 mg mL^{-1} as stock solution and then diluted to 0.3 mg mL^{-1} for measurement. Secondary structure analysis was performed using the CONTIN-LL and CDSSTR algorithms provided by DICHROWEB (http://dichroweb.cryst.bbk.ac.uk/html/home.shtml).[28]

Thermal shift assay

Peptide solutions were maintained at 20 μM (final concentration) in HBS (20 mM HEPES, pH7.3, 150 mM NaCl). SYPRO Orange (S5692, Sigma-Aldrich) was used at a final concentration of 5X. Experiments were carried out using clear 96-well PCR plates (MLL9601; Biorad, Hercules, CA) and each plate was sealed with Microseal PCR plate film (MBM1001, Bio-Rad). Each sample was divided into three 25 μL replicates. After centrifugation at 2000xg for 2 min at RT, plates were loaded onto the CFX Connect real-time PCR detection system (Bio-Rad). Fluorescence intensity was measured via SYPR PrimePCR chemistry in the FRET channel using the following protocol: 25°C for 2 min, then the temperature was continuously increased from 25°C to 95 °C at a heating rate of 1 °C min^{-1}. Melt Curve Results (Derivative & RFU) were directly exported from the instrument and analyzed with GraphPad Prism.

Peptide crosslinking & SDS-PAGE

NTE peptides (100 μM in 20 mM HEPES, pH7.3, 150 mM NaCl) in the absence or presence of PIP_3 (50 μM) were incubated with 1 mM of glutaraldehyde (G7651, Sigma) at room temperature for 8–10 min (all concentrations are the final concentrations of the mixture). NuPage LDS 4x sample buffer (in Tris-HCl pH8.5) was added to quench the crosslinking reaction and subjected to SDS-PAGE (10% Bis-Tris gel with MES-SDS running buffer pH7.2, Thermo Fisher Scientific) and Coomassie Blue (G-250) staining.

Mass spectrometry

Harvested cells were lysed by sonication in 2.5 volumes of lysis buffer containing 25 mM Tris pH7.5, 1 mM EDTA, 0.5% NP-40, 0.1% CHAPS and 150 mM KCl. The lysate was cleared by centrifugation at 100K g and the supernatant was used for immuno-purification using anti-DIRAS3 polyclonal antibody generated in our laboratory. The affinity purified DIRAS3 proteins were digested on beads. The beads were washed with cold PBS twice, resuspended and digested with 500 ng of trypsin (T9600, Gendepot) for 3 h. The digested peptide was enriched with an in-house STAGE tip (PMID: 12585499) column with 2 mg of C18 beads (3 μm, Dr. Maisch GmbH, Germany) and vacuum dried. Resuspended peptides were subjected to a nanoLC-1000 (Thermo Scientific) coupled to Orbitrap Fusion mass spectrometer (Thermo Scientific) with ESI source. The peptides were loaded onto an in-house Reprosil-Pur Basic C18 (1.9 μm, Dr. Maisch GmbH, Germany) trap column (2 cm length, 100 μm i.d.) and separated by 5 cm column (150 μm i.d.) with a 75 min gradient of 0–35% of acetonitrile/0.1% formic acid at a flow rate of 800 nL min^{-1}. The data acquisition was made in a data dependent analysis mode (DDA) for unbiased peptide detection and targeted parallel reaction monitoring mode (PRM) for deep monitoring of myristoylated N-terminal peptide. For the DDA mode, precursor MS spectra were scanned at 300–1400 m/z, 120k resolution at 400 m/z, $7.5x10^5$ AGC target (50 ms maximum injection time) by Orbitrap. Top 2 s cycle time was applied to selected MS1 signal and filtered by Quadrupole (1.6 m/z isolation window, 15 s exclusion time), fragmented by Higher-energy C-trap dissociation (HCD) and detected by Ion trap with rapid scan rate ($5x10^3$ AGC target, and 35 ms of maximum injection time). For PRM mode to detect N-terminal glycine myristylation the target m/z was 489.2914 (+2 charge, myr-GNASFGSK). Pre-selected precursor ions were scanned for 0 to 75 min of MS run time and isolated by quadrupole followed by collision-induced dissociation (CID) MS2 analysis. Obtained spectra were searched against the target-decoy Human RefSeq database (release 2020) in Proteome Discoverer 2.1 interface (PD 2.1, Thermo Fisher) with the Mascot algorithm (Mascot 2.4, Matrix Science). Dynamic modifications of the myristoylation on N-terminal glycine, acetylation of N-terminus and oxidation of methionine were allowed. The precursor mass tolerance was confined within 20 ppm with fragment mass tolerance of 0.5 Da and a maximum of two missed cleavages was allowed. Assigned peptides were filtered with 1% false discovery rate (FDR) using percolator validation based.

Computational analysis and molecular docking

DIRAS3 NTE wild type and mutant structures were predicted using the Phyre2 program as implemented at http://www.sbg.bio.ic.ac.uk/phyre2.[29] Intensive mode was used for all predictions. PIP_3 structure was prepared as sketched 2D molecules in KingDraw and energy-minimized in MOE version 2019.0102 to produce 3D structures. Energy minimization was performed using the Amber10:EHT force field with the RMS gradient set to 0.001 kcal/mol/A^2. Docking of PIP_3 molecules into DIRAS3 NTE structures and subsequent analysis was performed in MOE version 2019.0102. DIRAS3 NTE structures were prepared using the Structure Preparation function, followed by energy minimization using the same settings as for the PIP_3diC_8 structures. For all DIRAS3 NTE structures, the docking site was set to be residues 12–29. Proxy triangle was used as the placement method, with affinity dG as the scoring function, while induced fit was employed as the refinement method, with GBVI/WSA dG as the scoring function. From the initial placement, the top 100 poses were kept for the refinement step, and then, the top 20 poses were output. PIP–DIRAS3 NTE interactions for the selected poses were analyzed using the Ligand Interactions function. All structures were visualized in PyMOL.

Molecular dynamic simulation

Prediction of NTE secondary structure using various algorithms including PEPFOLD[30] (http://bioserv.rpbs.univ-paris-diderot.fr/services/PEPFOLD/) yielded a helix-loop-helix motif in which a cluster of hydrophobic residues is flanked by clusters of basic residues, consistent with the above structural analysis. We then ligated this structure to the core of the catalytic domain that has been modeled using DIRAS1/2 structures (PDB ID 2GF0 and 2ERX, respectively) as template, and added the flexible C-terminal domain along with the geranylgeranylated chain at residue 226. The resulting full-length protein was attached to a phosphatidylcholine/phosphatidylserine bilayer as described in previous studies on RAS proteins.[31–33] After adding water molecules and ions, we conducted multiple runs of ~200 ns molecular dynamics (MD) simulations, following previously described protocols.[31,32]

Immunofluorescence staining

Cells on 22 × 22 mm coverslips were fixed in 4% formaldehyde in PBS (Thermo Fisher, J19943-K2) and permeabilized with 0.1% Triton X-100 (Sigma, X100) in PBS for 15 min. Cells were blocked with 5% BSA in PBS for 30 min and then stained with antibody overnight at 4°C, followed by secondary antibody and DAPI for 1 h. Coverslips were mounted with Fluoro-Gel with TES buffer (Electron Microscopy Sciences, 50-246-96) and air dried. DIRAS3 membrane localization was evaluated. DIRAS3 inducible Cells (OVCAR5, OVCAR8 and SKOv3) were treated with doxycycline to induce DIRAS3 expression. After 24-h incubation, cells were fixed. Cells were stained with the antibodies as indicated. Images were captured using an Olympus Model IX71.

Clonogenic assay

HEK293 human embryo kidney cells were grown at 37°C to near confluence in Dulbecco's modified Eagle's medium containing 10% fetal bovine serum. Cells were transfected with plasmids containing wild-type and mutant DIRAS3-related sequences in pcDNA3.1(+) vectors using Lipofectamine (Bio-Rad) as described by the supplier. At 4 h after transfection, the medium was replaced with Dulbecco's modified Eagle's medium with 10% fetal bovine serum. After incubation for 24 h at 37°C, transfected cells were trypsinized and seeded into 6-well plate in triplicate. Selection medium with G418 (200 μg/mL) was added. After 2 weeks, colonies were stained with 0.1% Coomassie blue in 30% methanol and 10% acetic acid and then counted.

Immunoblotting

To evaluate the transfection efficiency of each construct, protein lysates were prepared 48 h post-transfection by washing the cells with ice-cold PBS and then suspending them for 1 min at room temperature in 150 μL of SDS lysis buffer containing 62.5 mM Tris-HCL pH 6.8, 2.5% SDS, 10% glycerol, 5% β-mercaptoethanol, and 0.002% bromophenol blue. Lysates were placed on a dry block at 99°C for 5 min. Subsequently, the whole cell lysates (15 μg of total protein) were separated by SDS-PAGE using 4–20% Mini-PROTEAN TGX Precast Protein Gels and transferred to PVDF membranes. Immunoblot analysis was performed with the primary antibodies (mouse monoclonal anti-DIRAS3, anti-β-actin, anti-vinculin), and secondary antibodies (HRP-conjugated anti-mouse and anti-rabbit) indicated and visualized with an ECL-enhanced chemiluminescence detection kit (SuperSignal West Pico PLUS, Thermo Scientific).

QUANTIFICATION AND STATISTICAL ANALYSIS

Statistical analyses were performed using GraphPad Prism. The statistical significance of the differences between the groups was investigated using one-way ANOVA. All experiments have been repeated a minimum of three times where samples were measured in technical triplicate.